JTTEE5 19:964–974
DOI: 10.1007/s11666-010-9480-5
1059-9630/$19.00 © ASM International

Microstructure and Wear Behavior of Conventional and Nanostructured Plasma-Sprayed WC-Co Coatings

E. Sánchez, E. Bannier, M.D. Salvador, V. Bonache, J.C. García, J. Morgiel, and J. Grzonka

(Submitted October 19, 2009; in revised form December 28, 2009)

WC-12%Co coatings were deposited by atmospheric plasma spraying using conventional and nanostructured powders and two secondary plasmogenous gases (He and H_2). Coating microstructure and phase composition were characterized using scanning electron microscopy (SEM), transmission electron microscopy (TEM), and x-ray diffraction techniques (XRD) techniques. This study examined wear and friction properties of the coatings under dry friction conditions. SEM was used to analyze abraded surface microstructure. Coating microhardness and fracture toughness were also determined. All coatings displayed strong decarburization as a result of WC decomposition, which gave rise to the formation of secondary phases (W_2C and W). A very fine undissolved WC crystalline dispersion coexisted with these new phases. TEM observation confirmed that the matrix was predominantly amorphous and filled with block-type, frequently dislocated crystallites. Wear was observed to follow a three-body abrasive mechanism, since debris between the ball and the coating surface was detected. The main wear mechanism was based on subsurface cracking, owing to the arising debris. WC grain decomposition and dissolution were concluded to be critical factors in wear resistance. The level of decomposition and dissolution could be modified by changing the plasmogenous gas or feed powder grain size. The influence of the plasmogenous gas on wear resistance was greater than the influence of feedstock particle size.

Keywords air plasma spraying, ball on disk, conventional coating, nanostructured coating, WC-Co, wear resistance

1. Introduction

Thermally sprayed WC-Co coatings have been widely used in many industries for applications where high wear resistance is required. The thermal spray process involves introducing feedstock powders into a high-temperature flame where they are rapidly melted and accelerated toward a substrate to form a coating. Coating wear performance depends on feedstock powder characteristics and thermal spray conditions. WC-Co powders are exposed to high-temperature flames that induce WC decomposition and dissolution. As a result, these coatings exhibit multiphase microstructures and are generally made up of lamellar splats, with WC crystals, secondary phases (W_2C and W), and an amorphous brittle Co-based binder phase (Ref 1, 2). As reported elsewhere, these secondary phases are detrimental to hardness, toughness, and wear resistance (Ref 3, 4). A coating with high tungsten monocarbide retention is therefore desirable.

Numerous studies have examined the relationship between feedstock powder characteristics, process conditions, microstructural parameters, and wear resistance of thermally sprayed WC-Co coatings (Ref 5-9). Starting powder chemistry, powder size, initial phase content, and carbide grain size have been found to determine phase distribution in the coating. The preferable morphology of these coatings, for good wear resistance, is reported to correspond to well-dispersed fine hard carbide particles (Ref 10). Although the most suitable technique for achieving this type of microstructure by thermal spraying is currently held by the high-velocity oxy fuel (HVOF) process (Ref 8), similar morphologies can also be obtained with other thermal spray processes (Ref 5).

Thermally sprayed coatings with a nanostructured WC-Co feedstock powder have been shown to exhibit enhanced wear resistance compared to that of spray coatings obtained with conventional WC-Co powders (Ref 10). Other reports, however, indicate that the use of feedstock powders with nanoscale carbides leads to excessive decomposition during thermal spraying, and thus to embrittled coatings with low wear resistance (Ref 11, 12). The foregoing findings for the abrasion response of thermally sprayed WC-Co coatings show a slight reverse trend compared to those obtained for sintered cermets (Ref 13, 14). Note, however, that there was a great difference in phase distribution among the coatings with different feedstock grain size in these studies.

E. Sánchez and **E. Bannier**, Instituto de Tecnología Cerámica – Asociación de Investigación de las Industrias Cerámicas, Universitat Jaume I, Castellón, Spain; **M.D. Salvador, V. Bonache,** and **J.C. García**, Instituto de Tecnología de Materiales, Universidad Politécnica de Valencia, Valencia, Spain; and **J. Morgiel** and **J. Grzonka**, Institute of Metallurgy and Materials Science, Kraków, Poland. Contact e-mail: emilie.bannier@itc.uji.es.

This study has sought to evaluate the influence of the plasmogen gas (H_2 or He) and powder size (micrometric or nanometric) on the microstructure and wear resistance of plasma-sprayed WC-Co coatings. Wear mechanisms were studied and the friction coefficient and wear rate were calculated of all the resulting coatings. A ball-on-disk tribometer was chosen, since this technique is widely used to determine coating friction and wear characteristics. Wear rate and the variation of the friction coefficient with distance can easily be obtained with this test.

2. Experimental Procedure

2.1 Materials

Two different types of WC-12%Co feedstock powders were used in this study: micrometric powder and nanometric powder. Certain powder characteristics provided by the suppliers are shown in Table 1.

2.2 Feed Powder Characterization

Both powders were fully characterized before deposition. The crystalline phases were first determined using x-ray diffraction (XRD) technique (Bruker D8). The powders were then observed by scanning electron microscopy (SEM) using a Jeol 6300 instrument.

2.3 Coating Processing

WC-Co coatings were deposited by a high-power atmospheric plasma spray (APS) system. The substrates (carbon steel plates) were grit-blasted with Al_2O_3 before the plasma spray application to clean and roughen the surface. The plasma spray system consisted of a Sulzer Metco F4-MB gun, operated by an ABB IRB 1400 robot. Ar was used as primary plasma gas, while H_2 and He were used as secondary gases. Spray conditions are detailed in Table 2.

2.4 Wear Testing

Wear tests were performed on the coatings, without lubrication, at room temperature using a ball-on-disk arrangement with a Microtest MT2/60/SCM/T tribometer. The wear tests were performed under two loads (20 and 50 N) with a sliding distance of 2000 m and a sliding speed of 0.1 m/s. Al_2O_3 and Si_3N_4 balls, 4 mm in diameter, were used in the tests. The Al_2O_3 and Si_3N_4 balls had a Vickers' microhardness (under indentation with 500 gf load) of 1380 and 1880 kgf/mm^2, respectively.

Before and after each wear test, the test pieces were cleaned by means of compressed air and brushing, and were held in ultrasound for 15 min. Mass loss was determined by sample weighing before and after the test, using a microbalance with an accuracy of ±0.1 mg. The wear rate (wr) was determined from the following equation:

$$wr = \frac{m}{L \cdot D}, \quad \text{(Eq 1)}$$

where m (kg) is sample mass loss, L (N) is the applied load, and D is the sliding distance (m).

2.5 Characterization of Coatings and Abraded Surfaces

The SEM instrument (Jeol 6300) and the field emission scanning electron microscope (HITACHI S-4100) equipped with an energy-dispersive x-ray spectrometer (EDS) were also used to study coating microstructure and to analyze the abraded surfaces. Two different cross-sections (about 15 × 2 mm^2) were observed for each type of coated sample. Coating microstructure was also examined with a PHILIPS CM20 transmission electron microscope (TEM). Thin foils were prepared using a focused ion beam system (FEI Dual Beam with Omniprobe pick-up systems) for the TEM observations.

To identify the phases present, XRD (Bruker D8) was performed on the surface of the as-sprayed coatings. Porosity was measured by image analysis of the optical micrographs. The Vickers microhardness tests were conducted using a Matsuzawa MHT2 micro-hardness tester at 500 g load and dwell time of 15 s. Microhardness values were determined by performing 10 indentations on each coating sample. Fracture toughness (K_{IC}) was estimated by the Vickers indentation technique at 1 kg load. The Lawn and Fuller equation was used to calculate toughness (Ref 15):

$$K_{IC} = 0.0515\frac{P}{c^{3/2}}, \quad \text{(Eq 2)}$$

where P is the applied load (N) and c is the crack length measured from the center of the indentation (m).

Table 2 Parameters used in plasma spraying

Ar, slpm	H_2, slpm	He, slpm	Intensity, A	Spraying distance, mm	Spraying velocity, mm/s	Mass flow, g/min
65	3	···	750	130	1000	50
60	···	120	625	110	1000	30

Table 1 Characteristics of the powders used (information provided by the suppliers)

Powder	Supplier	Reference	Composition	Powder agglomerate size, µm
Conventional	Sulzer Metco (Hattersheim, Germany)	72F-NS	WC-12Co	15-45
Nanometric	Inframat Advanced Materials (Willington, USA)	Infralloy S7412	WC-12Co	5-45

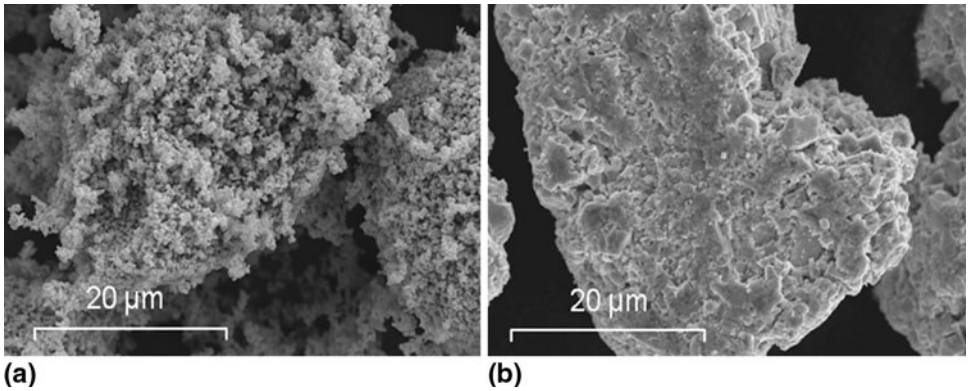

Fig. 1 SEM micrographs of the powders used: (a) micrometric and (b) nanometric

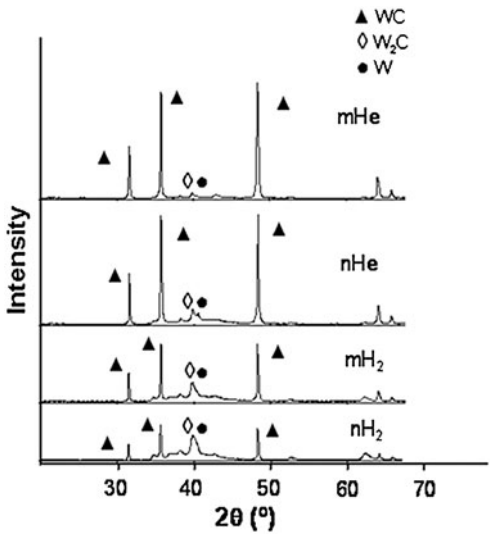

Fig. 2 XRD scans for coatings sprayed using micrometric powder and H_2 (mH_2), micrometric powder and He (mHe), nanometric powder and H_2 (nH_2), and nanometric powder and He (nHe)

3. Results and Discussion

3.1 Characterization of the Feed Powders

The SEM micrographs of feed powder morphology are shown in Fig. 1. The micrometric powder displayed the typical morphology of thermal spray feedstock, consisting of dense agglomerates, about 40 to 50 μm in size. In contrast, the nanometric powder consisted of porous agglomerates, containing particles ranging from 50 to 500 nm in size.

SEM observations confirm the different routes followed to obtain the powders. The micrometric powder was obtained by a traditional melting and crushing procedure, while a reconstitution process, basically comprising a granulation step followed by thermal treatment, was probably used to prepare the nanometric feed powder. The thermal treatment of the nanometric agglomerates before thermal spraying is confirmed by the sintering state exhibited by the microstructure in Fig. 1.

XRD of the feedstocks showed that WC and Co were the main constituents in both powders.

3.2 Microstructural Characterization of the Coatings

The XRD analysis of the as-sprayed cemented carbide coatings, obtained with both conventional and nanostructured powders, sprayed either in H_2 or He, is presented in Fig. 2. It shows that the coatings are constituted by three crystalline phases (WC, W_2C, and W). WC is present in the initial powder, but the other two phases have been formed in the spraying process through WC particle decarburization (Ref 2, 16). A hump indicating the presence of amorphous or nanocrystalline material was observed in all cases.

In general, the coatings obtained using He as secondary gas displayed less decomposition than the coatings sprayed with H_2, evidenced by weaker W_2C and W peaks in the XRD spectra (Fig. 2). This can be explained by the lower energy of the plasma plume when He was used as secondary gas and by the much higher gas flow rates, which provide higher plasma density and restrict oxygen entry into the flame. The substitution of agglomerated nanostructured powders for conventional powders also led to higher decarburization, though the decomposition was smaller than that observed in the XRD spectra when the secondary plasmogenous gas was changed.

SEM observations of the coatings revealed the presence of all the phases detected by XRD. Moreover an amorphous Co-rich matrix was identified. They had about 10% porosity and were about 200 μm thick. Observation of the coatings with backscattered electron (BSE) imaging confirmed the presence of the crystalline phases detected by XRD (WC, W_2C, and W) and a Co-rich matrix phase to be identified (Fig. 3).

It has been reported elsewhere that Co melts during spraying followed by dissolution of some WC grains into the liquid metal (Ref 17). When the sprayed material

impacts and cools, W_2C and W (in addition to WC) may precipitate from the liquid with any remaining liquid forming an amorphous matrix containing W, C, and Co (Ref 7). A Co-rich phase with regions of differing composition thus forms in the end coating.

In the SEM images, the bright areas belong to matrix areas with high W content (element with the higher mean atomic number). The WC grains are located inside the ''splats,'' in which the temperature reached during spraying was not high enough to dissolve the grains. W_2C was identified around the WC grains, while W was detected in the outer part of the splats, in which the degree of decarburization was higher. A larger Co-rich matrix was found in the coatings sprayed using H_2 and nanometric powder. When H_2 was used, the resulting plasma was more energetic, and the particle temperature in the plasma jet was higher. This encourages WC particle dissolution, increasing the Co-rich region (as can be seen in Fig. 4 in the nanostructured case). When nanometric powder was used, a slightly higher dissolution of the WC particles also occurred owing to the higher surface-volume ratio. SEM observation also showed that, in the nanometric coatings, the WC grains were smaller (Fig. 5).

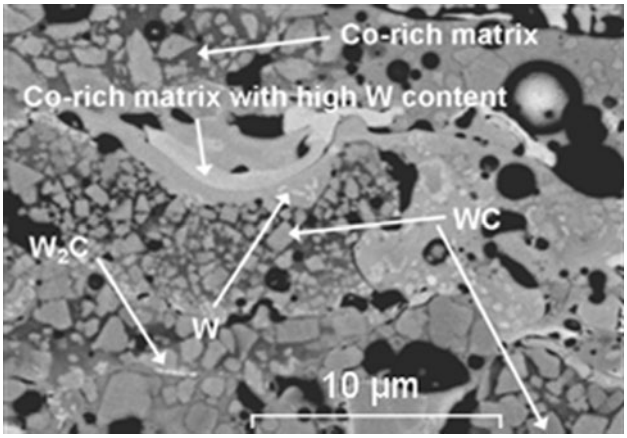

Fig. 3 SEM micrographs showing the general microstructure of mH_2 coating. The main areas identified by EDX are indicated

The TEM observations focused on the areas containing fine dispersions of WC crystals in the Co-rich matrix. Figure 6 shows that the matrix is predominantly amorphous and filled with block-type, frequently dislocated crystallites. In addition to the block-type WC crystallites, some rounded or elongated particles are also present, indicating partial particle melting during the APS process. The analyzed areas also display a high density of spherical or elongated voids. Detailed microstructural observations showed that, in addition to the amorphous matrix with crystalline WC, there were also areas in which the matrix had begun to transform into a nanocrystalline phase, as documented in Fig. 7 for the conventional coating. Electron diffraction confirmed locally a fully amorphous structure of the matrix and the presence of WC crystals. These observations indicate that the nanostructured coatings also contain amorphous areas differing significantly in contrast, as shown in Fig. 8. Since the thin foils were prepared using the FIB technique, which allows producing specimens of approximately the same thickness, such differences in contrast can only be attributed to variations in material density, i.e., the presence of amorphous material of varying composition (see Fig. 8, regions labeled X and Y).

3.3 Mechanical Properties of Coatings

The Vickers microhardness and toughness values obtained for each coating are shown in Fig. 9. For both gases, the highest microhardness was obtained when nanometric powder was used. The coatings sprayed with He exhibited much higher toughness values and slightly higher hardness values than the coatings sprayed with H_2. The effect of powder size on toughness is not too clear.

The highest microhardness values were obtained when nanometric powder was used. This could be due to the presence of a larger W_2C content (phase harder than WC),

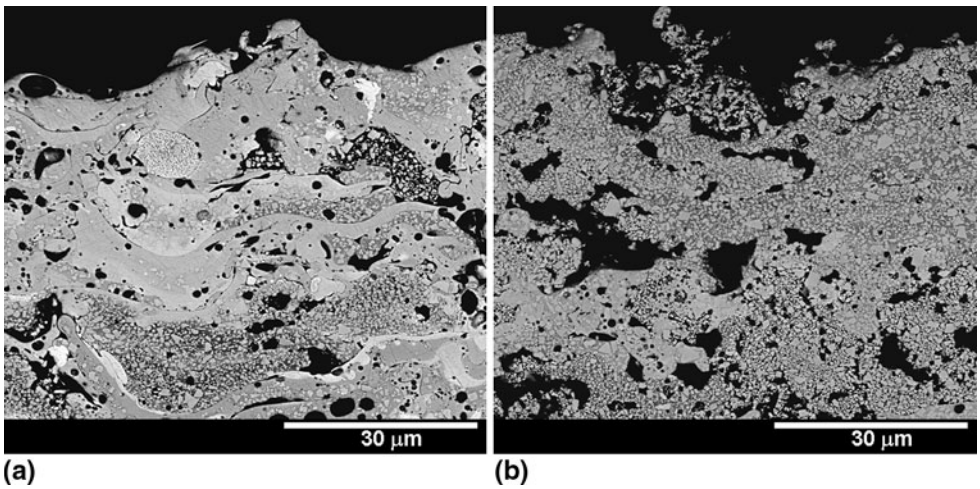

Fig. 4 FESEM micrographs showing general microstructure of (a) nH_2 coating and (b) nHe coating

Co matrix hardening by W dissolution, and smaller WC grain size. The effect of grain size on microhardness for sintered materials is described elsewhere (Ref 18), though this effect is not as clear in coatings as in bulk material. The gas used also has a great influence on the resulting microhardness values. When He was used, higher microhardness values were obtained because the coatings sprayed using He displayed a microstructure with more WC grains. Since the He plasma gas was less energetic, WC decomposition and dissolution decreased, thus enabling a larger number of WC grains to be retained in the coating microstructure. An increase in microhardness is to be expected when the WC grain content in the coating microstructure is larger (Ref 19). In addition, the highest toughness values were obtained when He was used. These values are similar to those found in HVOF spray coatings (Ref 20). When H_2 was used, the Co matrix contained more regions in which the WC grains had completely dissolved. These regions are more brittle and cracks can therefore propagate more readily.

3.4 Wear and Tribological Behavior

The wear rates of the four WC-12Co coatings obtained by using Al_2O_3 and Si_3N_4 balls, loading at 20 and 50 N, are shown in Fig. 10. The wear rate of the coatings sprayed with H_2 is observed to be significantly higher for the two test balls and for the two applied loads. The wear rates in the coatings sprayed with H_2 were generally higher when Al_2O_3 was used, while in the coatings sprayed with He, the highest wear rates were obtained using Si_3N_4 balls. Generally, the wear rates obtained are 10 times higher than those obtained by Qiao et al. in sliding wear tests conducted on a ball-on-disk tribometer without lubrication using Si_3N_4 ball (Ref 21). However, wear rates are approximately 5000 times lower than wear rates obtained by the same authors in abrasion tests. Note, furthermore, that the wear rate increases with load in micrometric coatings and decreases in nanometric coatings. This tendency was also observed by Zhu et al. (Ref 22) in sliding wear tests under dry friction conditions, using Al_2O_3 ball

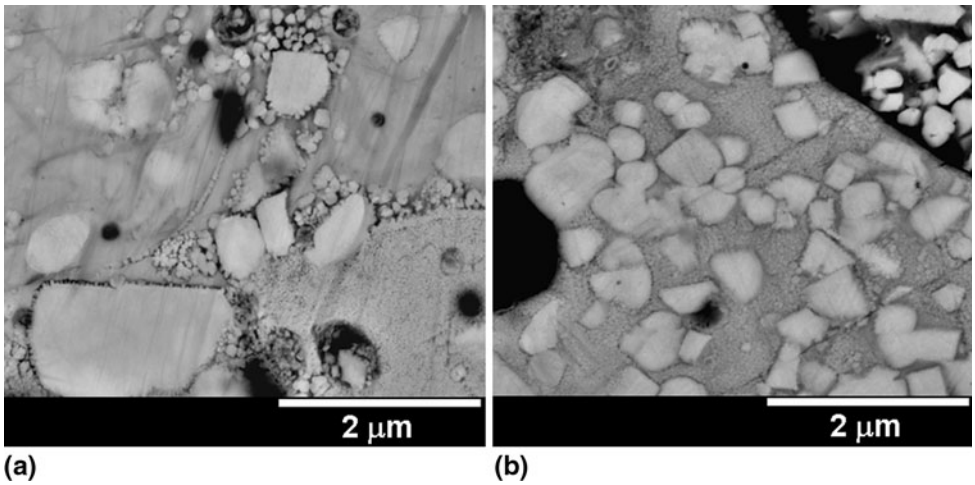

Fig. 5 FESEM micrographs showing high magnifications microstructures of dispersions of WC crystals found in (a) mHe coating and (b) nHe coating

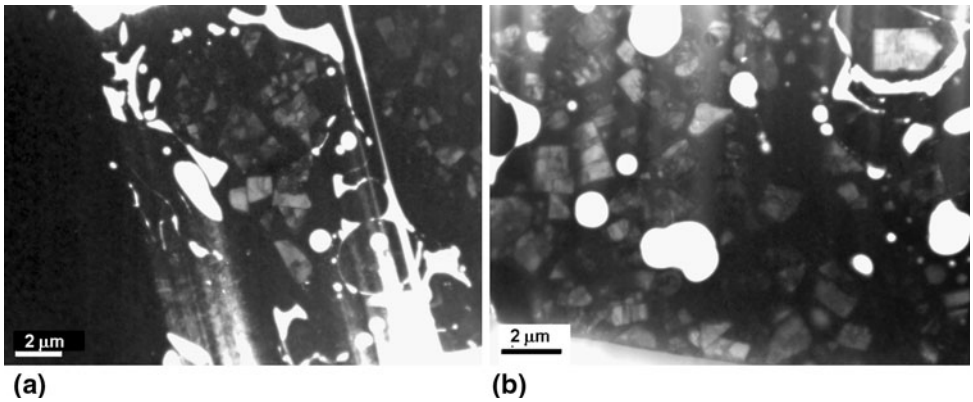

Fig. 6 TEM micrographs of WC-Co coatings showing WC crystals in a mostly amorphous Co matrix in an (a) mH_2 coating and (b) nH_2 coating

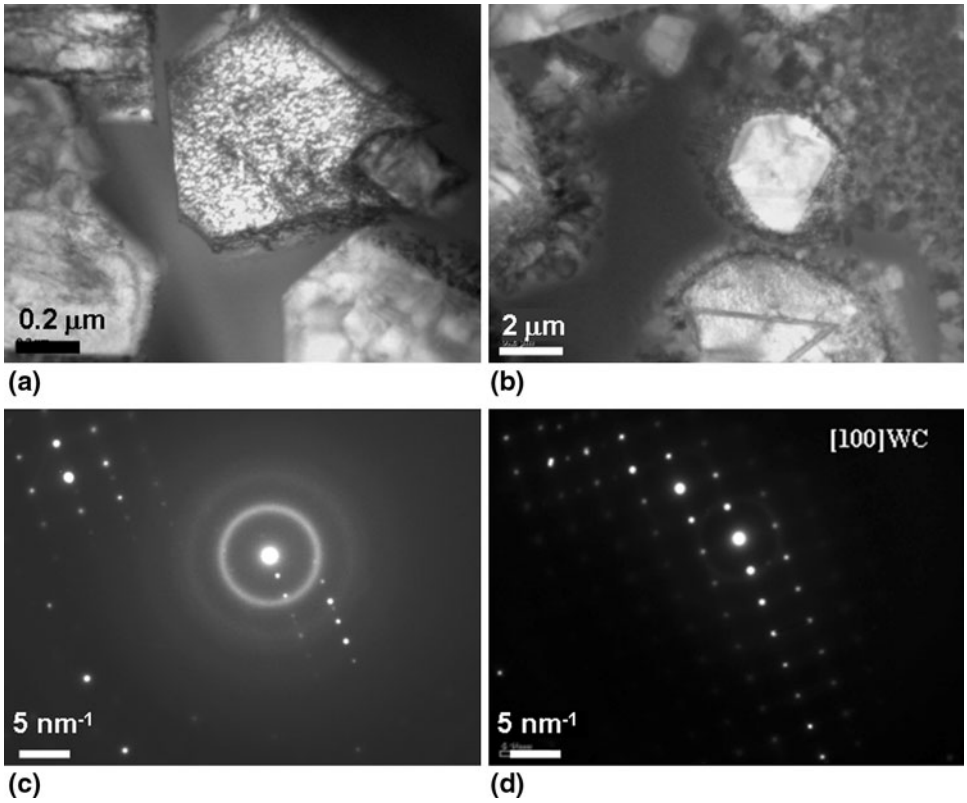

Fig. 7 TEM micrographs of mH_2 displaying: (a) WC in an amorphous matrix, (b) an amorphous/nanocrystalline matrix, and diffractions from (c) an amorphous matrix and (d) WC

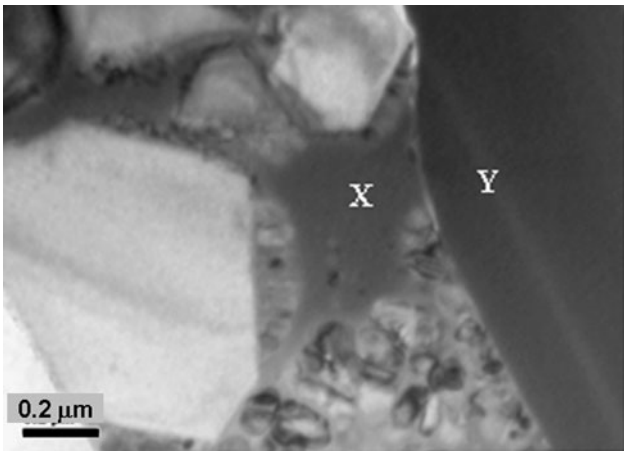

Fig. 8 TEM micrograph of an nH_2 coating displaying WC in an amorphous/nanocrystalline matrix. The differences in contrast between regions X and Y indicate variations in material density, e.g., the presence of amorphous material of varying composition

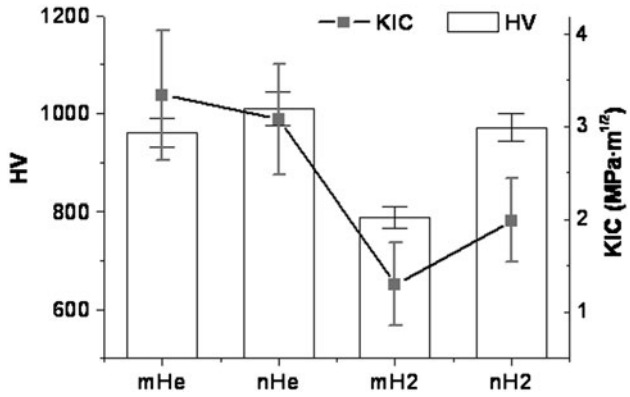

Fig. 9 Vickers microhardness and toughness values of the studied coatings

as counterface. Moreover, these authors established that the wear rate of conventional coatings augmented from 6.5×10^{-7} to 23×10^{-7} mm^3/Nm when load was raised from 20 to 40 N. However, in nanometric coatings, they found that wear rate did not appreciably change with load. In Fig. 10 it can be observed that, when He is used, conventional coatings present a higher wear rates than nanometric coatings. This result is in accordance with others studies (Ref 22, 23), which also showed that nanometric WC-Co coatings exhibit better wear resistance than micrometric ones.

The friction coefficients of the four WC-Co coatings are presented in Fig. 11, and Fig. 11(b) shows that the friction coefficients of the coatings against Al_2O_3 are very similar and increase when the applied load is raised from 20 to 50 N. Greater differences are observed, however, with the Si_3N_4 ball (Fig. 11a), the friction coefficient for the

micrometric coatings generally being lower. Note, furthermore, that in the coatings sprayed with H_2, the friction coefficient decreases significantly with the applied load, whereas load does not have a significant effect on the friction coefficient of the coatings sprayed with He.

In most test conditions, no marked relationship between wear rate and friction coefficient was found. The only exception concerned tests conducted at 20 N, using Si_3N_4 ball. In such situation, the evolution of friction coefficient and wear rate present a similar tendency, as can be observed comparing Fig. 10 and 11. In other words, if friction coefficient increases, wear rate also increases. The same trend was observed by Zhu et al. (Ref 22) in sliding tests conducted at 20 N under dry friction conditions using Al_2O_3 balls. However, these authors found an opposite tendency at higher loads (40 and 60 N).

As it was mentioned above, the variation of the friction coefficient with the applied load differs for the two test balls. The friction coefficient increased with the applied load when the Al_2O_3 ball was used, whereas for coatings sprayed with H_2, the friction coefficient decreased with the applied load when the Si_3N_4 ball was used. This tendency can also be observed in Fig. 12, in which the friction coefficient is plotted against distance for the coatings sprayed using micrometric powder and H_2. If the unsteady initial period is disregarded, the friction coefficient is observed to increase with distance when the coatings are tested against Si_3N_4, while the opposite effect is noted

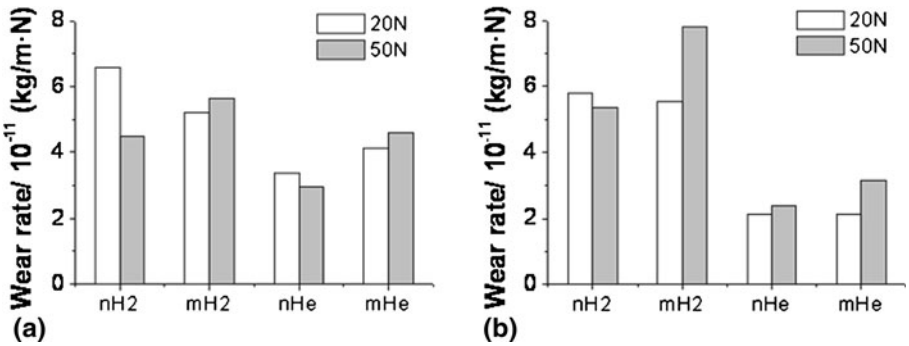

Fig. 10 Coating wear rates using: (a) Si_3N_4 ball and (b) Al_2O_3 ball

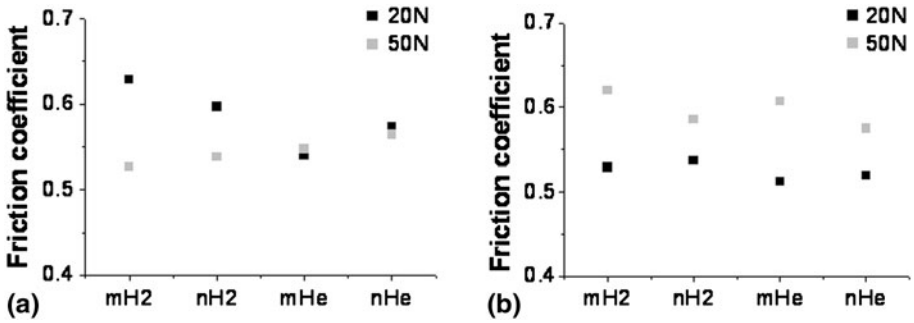

Fig. 11 Friction coefficients of WC-Co coatings using: (a) Si_3N_4 ball and (b) Al_2O_3 ball

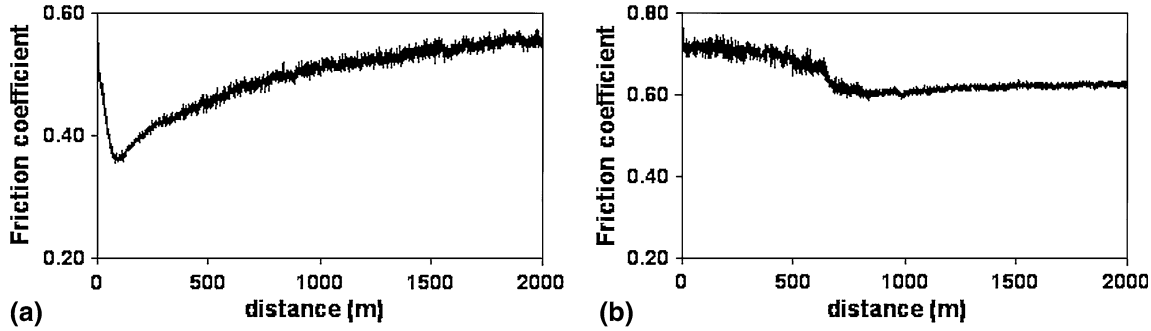

Fig. 12 Variation of the friction coefficient with distance for the mH_2 coating at 50 N using: (a) Si_3N_4 ball and (b) Al_2O_3 ball

when they are tested against Al_2O_3. This is because the load acting on the sample changes, owing to the change in surface contact between the ball and the sample. Ball wear causes the contact surface between the ball and the sample to increase with distance, so that the pressure in N/m^2 on the sample decreases. As a result, the variation in the friction coefficient obtained in Fig. 12 matches with the variation in friction coefficient found when the load was changed from 20 to 50 N (see Fig. 11).

It is important to point out that both balls used in sliding tests (Al_2O_3 and Si_3N_4) display a higher microhardness than the coatings. Besides, debris was detected between the ball and the coating surface, which suggests that wear generally occurred by a three-body abrasive mechanism. This debris, with grain sizes ranging from about 200 nm to 15 μm, stems from ball wear and WC grain pull-out and fragmentation. This mode of abrasive wear is different from the one observed in conventional abrasion tests (Ref 7, 21, 23, 24) where larger abrasive particles produce more severe wear (higher wear rates and different wear tracks). Qiao et al. found that abrasive wear is about 50,000 times higher than sliding wear (Ref 21). This huge difference is due to both size and quantity of the particles rolling in between the two surfaces in motion. In conventional abrasion wear testing, abrasive particles are much larger than the debris generated in sliding wear tests. Stewart et al. (Ref 7) have shown that the wear rate significantly increases with the abrasive size.

Removal of the Co-rich matrix was the first wear phase. SEM observation of the abraded surfaces shows individual WC grains (bright areas) standing in relief, apparently on the surface, indicating that the Co-rich matrix around the WC grains has been partly removed (Fig. 13a, b). WC grain scratching and fragmentation was also observed in the coatings, as shown in Fig. 13(a) and (b). This wear mechanism takes place predominantly in the largest grains and is, therefore, more common in the conventional coatings. Groove formation on the coating surface is shown in Fig. 13(c), indicating that the grooves are caused by displacement of the WC particle.

Grooving was observed to be more important in nanometric coatings. These results agree with that of Zhu et al. who put in evidence rather different wear mechanisms for nanostructured and conventional WC-Co coatings (Ref 22). Under mild testing conditions, these authors found that nanometric WC-Co coatings undergo plastic deformation and wear on a microscale, forming a smooth surface. In the conventional case, no grooves were detected in the wear scar, indicating that no plastic deformation occurred. Three-body abrasion mechanism was also observed by Zhu et al. on conventional WC-Co coatings in ball-on-disk tests using Al_2O_3 ball as counterface. In such situation, the fragmentation of WC grains under heavy loads is severe, and the fractured grains act as abrasives and origin three-body abrasion.

Wear was also observed to occur by subsurface cracking, which is a classical surface fatigue phenomenon. During sliding, contacts between asperities accompanied by very high local stresses are repeated several times. As a consequence, wear particles are generated by fatigue

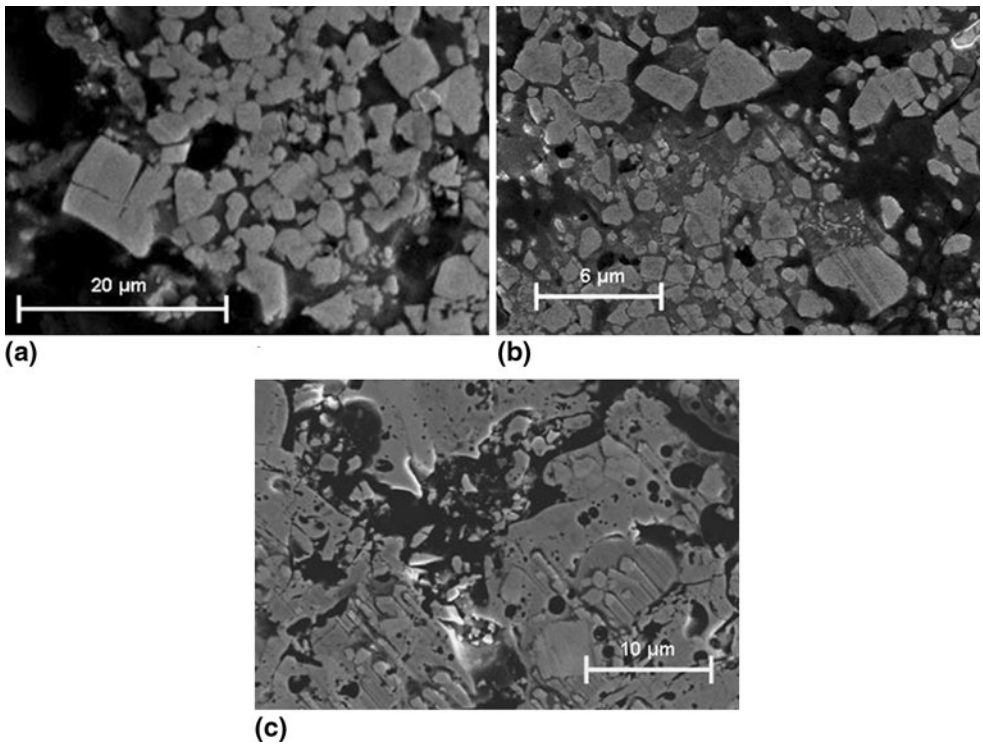

Fig. 13 SEM micrographs of wear scars for: (a) mHe coating, load 50 N, Al_2O_3 ball, (b) mHe coating, load 20 N, Si_3N_4 ball, and (c) mH_2 coating, load 20 N, Si_3N_4 ball

propagation of cracks. This mechanism can be observed in Fig. 14, which shows the removal of a large coating area due to the formation and propagation of subsurface cracks. First, a crack appears at the surface at some weak point and this primary crack propagates predominantly through the W-rich binder phase or along splat boundaries, as illustrated by Stewart et al. (Ref 7). Then, a secondary crack can grow from the primary crack; alternatively, the primary crack can connect with an existing subsurface crack. When the resulting crack reaches the surface again, a wear particle is released. The generation and propagation of cracks is mainly dependent on the intersplat cohesive strength of the coating (Ref 24). SEM observation showed that this phenomenon was the main material removal mechanism for all studied coatings. This mechanism occurred more frequently in coatings sprayed using H_2, as a higher content of W-rich binder areas (brittle phase) are found in these coatings. For coatings that suffered much decarburization, Qiao et al. also observed material removal due to fracture along cracks propagated by fatigue, as a consequence of the successive passages of the slider (Ref 21). In contrast, these authors found that in coatings which suffered relatively low decarburization wear occurs by attrition of individual grains.

The gas used had a greater effect on wear rate than feed powder grain size: wear resistance improved significantly with He. As noted above, when He was used, the resulting plasma jet was less energetic, so that WC particle

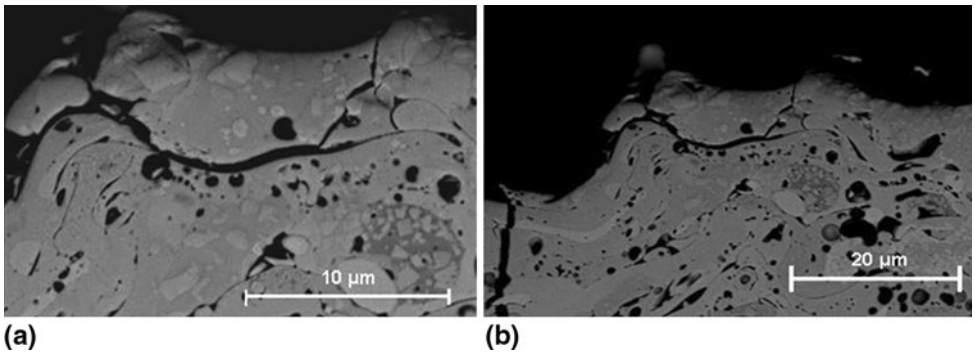

Fig. 14 SEM micrographs of the nH_2 coating using the Al_2O_3 ball at 50 N: (a) high magnification and (b) low magnification

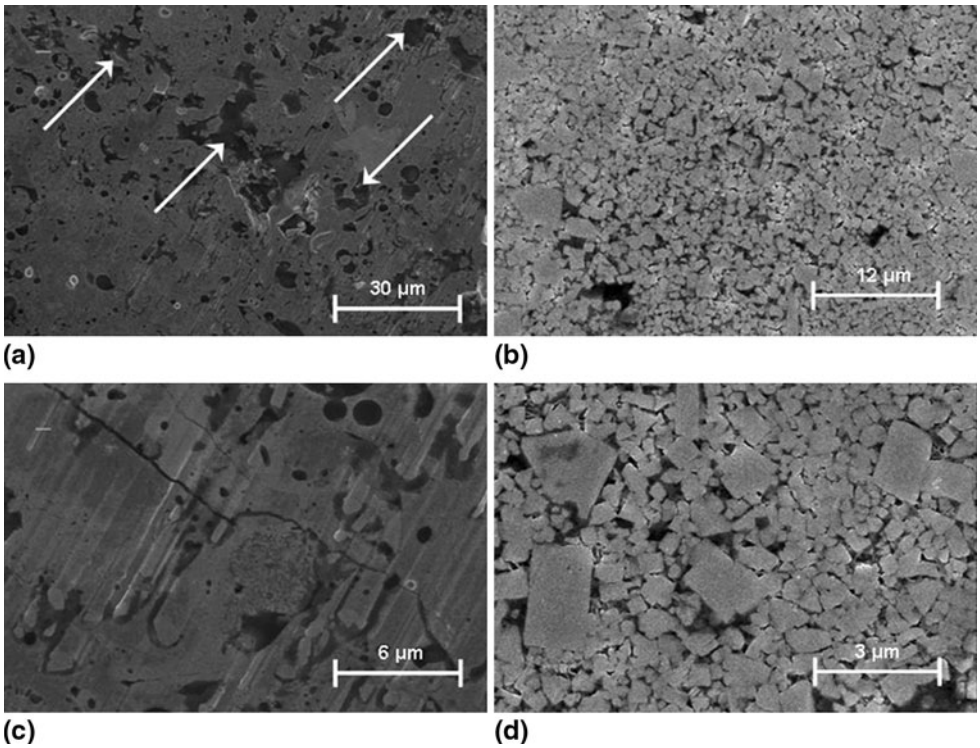

Fig. 15 FESEM micrographs of wear scars using the Si_3N_4 ball at 20 N for: (a) nH_2 coating (low magnification), (b) nHe coating (low magnification), (c) nH_2 coating (high magnification), and (d) nHe coating (high magnification)

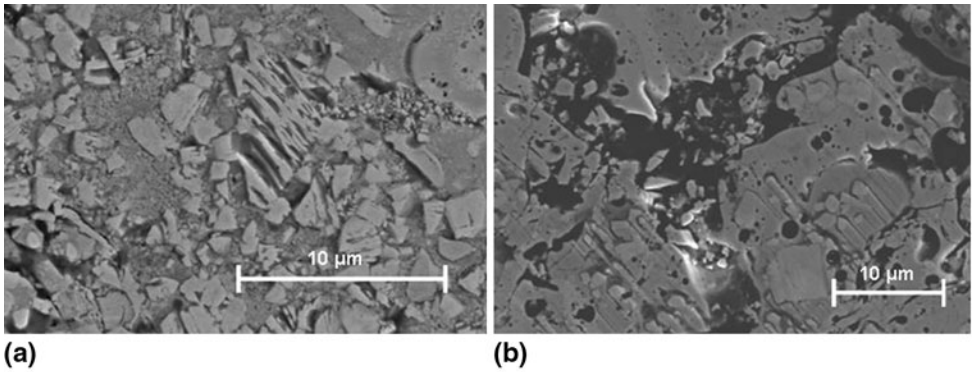

Fig. 16 FESEM micrographs of wear scars for: (a) mH_2 coating, 50 N, Al_2O_3 ball and (b) mH_2 coating, 50 N, Si_3N_4 ball

dissolution and decarburization decreased. A high level of WC was therefore retained in the coating. Similar trends were observed by Khan and Clyne (Ref 25) in air plasma-sprayed WC-Co coatings, in which increased plasma power (and, hence, increased WC grain decomposition during spraying) led to significant decreases in coating wear resistance. Figure 15 displays abraded surfaces of nanometric coatings sprayed with H_2 and He. Only the abraded surfaces of nanometric coatings, obtained using a load of 20 N and Si_3N_4 ball, are shown, but the results can be extrapolated to all the studied coatings. Very different wear mechanisms are to be observed between the two types of coatings. The H_2 coatings exhibit many grooves produced by WC grain displacement, with crack development perpendicular to the wear direction (Fig. 15a, c). In addition, more coating regions have been removed by subsurface cracking (marked by white arrows in Fig. 15a). No cracks formed in the He coatings, however, and there were fewer grooves. The main wear mechanism in Fig. 15(b) and (d) was the removal of the Co-rich matrix. It may further be noted in regard to Fig. 15 that, as mentioned above, He coating microstructure displayed more retained WC. This is the main cause of the differences in wear performance between the coatings sprayed with H_2 and those sprayed with He.

There were no significant differences in wear mechanisms when the Al_2O_3 ball or the Si_3N_4 ball was used. Subsurface cracking was the main wear mechanism in all coatings for both balls. Groove formation was more significant, however, when Si_3N_4 was used, while WC scratching and fragmentation was more significant when Al_2O_3 was used. Figure 16 presents two SEM images showing these differences in wear mechanisms.

As mentioned above, groove formation is more significant when the test is conducted against Si_3N_4 ball. This could be explained by the higher microhardness of the Si_3N_4 ball compared to Al_2O_3 ball (1880 against 1380 kg/mm^2). Indeed, abrasion wear behavior of coatings strongly depends on the ratio between coating and abrasive hardnesses (Ref 26). Besides, differences in debris particle morphology between tests conducted with Al_2O_3 and Si_3N_4 balls (observed by SEM) could also explain the different wear behavior.

4. Conclusions

In this study, two plasmogenous gases, H_2 and He, were used to obtain APS coatings from conventional and nanostructured WC-Co powder feedstocks. The study showed that the gas used in APS influences wear resistance more than grain size. The plasma jet produced using He is less energetic, thus reducing WC particle dissolution and decarburization and increasing the level of retained WC in the coating. Owing to the larger WC region, the coatings sprayed with He displayed the highest hardness and toughness values and the best wear resistance.

The main wear mechanism in all coatings was subsurface cracking, followed by subsequent material removal. Other secondary mechanisms such as removal of the Co-rich matrix, followed by WC scratching, fragmentation, and pull-out could also be observed. When He was used in plasma spraying, the coatings deposited with nanometric powder exhibited better wear resistance than the coatings sprayed with micrometric powder for all test loads and balls. This tendency runs counter to that reported elsewhere for thermally sprayed WC-Co coatings.

Acknowledgments

The authors gratefully acknowledge the financial support of the Ministry of Education and Science under project MAT 2006-12945 and of the EU under the network of excellence ''Knowledge-based Multicomponent Materials for Durable and Safe Performance'' (KMM-NoE, NMP3-CT-2004-502243).

References

1. C.J. Li, A. Ohmori, and Y. Harada, Effect of Powder Structure on the Structure of Thermally Sprayed WC-Co Coatings, *J. Mater. Sci.*, 1996, **31**, p 785-794
2. C. Verdon, A. Karimi, and J.L. Martin, A Study of High Velocity Oxy-Fuel Thermally Sprayed Tungsten Carbide Based Coatings. Part 1: Microstructures, *Mater. Sci. Eng. A*, 1998, **246**(1-2), p 11-24
3. Y. Qiao, T.E. Fischer, and A. Dent, The Effects of Fuel Chemistry and Feedstock Powder Structure on the Mechanical and

Tribological Properties of HVOF Thermal-Sprayed WC-Co Coatings with Very Fines Structures, *Surf. Coat. Technol.*, 2003, **172**(1), p 24-41
4. J. He, E.J. Lavernia, Y. Liu, Y. Qiao, and T.E. Fischer, Near-Nanostructured WC-18 pct Co Coatings with Low Amounts of Non-WC Carbide Phase: Part II. Hardness and Resistance to Sliding and Abrasive Wear, *Metall. Mater. Trans. A*, 2002, **33**(1), p 145-157
5. H. Liao, B. Normand, and C. Coddet, Influence of Coating Microstructure on the Abrasive Wear Resistance of WC/Co Cermet Coatings, *Surf. Coat. Technol.*, 2000, **124**(2-3), p 235-242
6. J. Voyer and B.R. Marple, Sliding Wear Behavior of High Velocity Oxy-Fuel and High Power Plasma Spray-Processed Tungsten Carbide-Based Cermet Coatings, *Wear*, 1999, **225-229**, p 135-145
7. D.A. Stewart, P.H. Shipway, and D.G. McCartney, Abrasive Wear Behaviour of Conventional and Nanocomposite HVOF-Sprayed WC-Co Coatings, *Wear*, 1999, **225-229**, p 789-798
8. Q. Yang, T. Senda, and A. Ohmori, Effect of Carbide Grain Size on Microstructure and Sliding Wear Behaviour of HVOF-Sprayed WC-12% Co Coatings, *Wear*, 2003, **254**, p 23-34
9. M.F. Morks, Y. Gao, N.F. Fahim, and F.U. Yingqing, Microstructure and Hardness Properties of Cermet Coating Sprayed by Low Power Plasma, *Mater. Lett.*, 2006, **60**(8), p 1049-1053
10. J. He and J.M. Schoenung, A Review on Nanostructured WC-Co Coatings, *Surf. Coat. Technol.*, 2002, **157**(1), p 72-79
11. A.H. Dent, S. De Palo, and S. Sampath, Examination of the Wear Properties of HVOF Sprayed Nanostructured and Conventional WC-Co Cermets with Different Binder Phase Contents, *J. Therm. Spray Technol.*, 2002, **11**(4), p 551-558
12. K.H. Baik, J.H. Kim, and B.G. Seong, Improvements in Hardness and Wear Resistance of Thermally Sprayed WC-Co Nanocomposite Coatings, *Mater. Sci. Eng. A*, 2007, **449-451**, p 846-849
13. K. Jia and T.E. Fisher, Abrasion Resistance of Nanostructured and Conventional Cemented Carbides, *Wear*, 1996, **200**, p 206-214
14. B.H. Kear and L.E. McCandish, Chemical Processing and Properties of Nanostructured WC-Co Materials, *Nanostruct. Mater.*, 1993, **3**(1-6), p 19-23
15. H.R. Lawn and E.R. Fuller, Equilibrium Penny-Like Cracks in Indentation Fracture, *J. Mater. Sci.*, 1975, **10**(12), p 2016-2024
16. J.M. Guilemany, J.M. de Paco, J.R. Miguel, and J. Nutting, Characterization of the W_2C Phase Formed During the High Velocity Oxygen Fuel Spraying of a WC + 12 Pct Co Powder, *Metall. Mater. Trans. A*, 1999, **30**(8), p 1913-1921
17. D.A. Stewart, ''Studies on the Abrasive Wear Behaviour of HVOF WC-Co Coatings,'' PhD Thesis, University of Nottingham, 1998
18. S.F. Wayne, J.G. Baldoni, and S.T. Buljan, Abrasion and Erosion of WC-Co Cermets with Controlled Microstructures, *Tribol. Trans.*, 1990, **33**, p 611-617
19. M.D.F. Harvey, A.J. Sturgeon, F.J. Blunt, and S.B. Dunkerton, Investigation into the Relationship Between Fuel Gas Selection, Wear Performance and Microstructure of HVOF-Sprayed WC-Co Coatings, *Thermal Spraying: Current Status and Future Trends*, A. Ohmori, Ed., May 22-26, 1995 (Kobe, Japan), High Temperature Society of Japan, 1995, p 471-476
20. S. Khameneh Aal, M. Heydarzadeh Sohi, K. Hokamoto, and M. Uemura, Effect of Heat Treatment on Wear Behavior of HVOF Thermally Sprayed WC-Co Coatings, *Wear*, 2006, **260**(11-12), p 1203-1208
21. Y. Qiao, Y. Liu, and T.E. Fischer, Sliding and Abrasive Wear Resistance of Thermal-Sprayed WC-CO Coatings, *J. Therm. Spray Technol.*, 2001, **10**(1), p 118-125
22. Y.C. Zhu, K. Yukimura, C.X. Ding, and P.Y. Zhang, Tribological Properties of Nanostructured and Conventional WC-Co Coatings Deposited by Plasma Spraying, *Thin Solid Films*, 2001, **388**(1-2), p 277-282
23. X.Q. Zhao, H.D. Zhou, and J.M. Chen, Comparative Study of the Friction and Wear Behavior of Plasma Sprayed Conventional and Nanostructured WC-12%Co Coatings on Stainless Steel, *Mater. Sci. Eng. A*, 2006, **431**(1-2), p 290-297
24. H.J. Kim, Y.G. Kweon, and R.W. Chang, Wear and Erosion Behavior of Plasma-Sprayed WC-Co Coatings, *J. Therm. Spray Technol.*, 1994, **3**(2), p 169-178
25. M.S.S. Khan and T.W. Clyne, Microstructure and Abrasion Resistance of Plasma Sprayed Cermet Coatings, *Thermal Spray: Practical Solutions for Engineering Problems*, C.C. Berndt, Ed., Oct 7-11, 1996 (Cincinnati, OH), ASM International, Materials Park, OH, 1998, p 113-121
26. G.W. Stachowiak and A.W. Batchelor, *Engineering Tribology*, Butterworth-Heinemann, Boston, 2001